Inhibitory cell type heterogeneity in a spatially structured mean-field model of V1

Soon Ho Kim* and Hannah Choi*
School of Mathematics
Georgia Institute of Technology
Atlanta, GA 30332-0160
(Dated: November 7, 2025)

Inhibitory interneurons in the cortex are classified into cell types differing in their morphology, electrophysiology, and connectivity. Although it is known that parvalbumin (PV), somatostatin (SST), and vasoactive intestinal polypeptide-expressing neurons (VIP), the major inhibitory neuron subtypes in the cortex, have distinct modulatory effects on excitatory neurons, how heterogeneous spatial connectivity properties relate to network computations is not well understood. Here, we study the implications of heterogeneous inhibitory neurons on the dynamics and computations of spatially-structured neural networks. We develop a mean-field model of the system in order to systematically examine excitation-inhibition balance, dynamical stability, and cell-type specific gain modulations. The model incorporates three inhibitory cell types and excitatory neurons with distinct connectivity probabilities and recent evidence of long-range spatial projections of SST neurons. Position-dependent firing rate predictions are validated against simulations, and balanced solutions under Gaussian assumptions are derived from scaling arguments. Stability analysis shows that while long-range inhibitory projections in E-I circuits with a homogeneous inhibitory population result in instability, the heterogeneous network maintains stability with long-range SST projections. This suggests that a mixture of short and long-range inhibitions may be key to providing diverse computations while maintaining stability. We further find that conductance-based synaptic transmissions are necessary to reproduce experimentally observed cell-type-specific gain modulations of inhibition by PV and SST neurons. These gain modulations are distance-dependent, and a linear response analysis suggested that shifts in the excitation-inhibition balance of the network underlie these effects. Our theoretical approach offers insight into the computational function of cell-type-specific and distance-dependent network structure.

I. INTRODUCTION

Cortical processing involves a precise interplay between synaptic excitation and inhibition [1–3]. Inhibitory neurons tune cortical oscillations, modulate gain, and gate excitatory neuronal responses [4–7]. Although cortical circuits are commonly modeled as recurrent neural networks [8], biological circuits have two features often overlooked in model networks: spatially-dependent connectivity [9] and the existence of cell types [10, 11].

Biological neural networks are spatially embedded, and distance plays an important role in governing connection probabilities [12]. To describe their effects on network dynamics, mean-field models of spatially distributed spiking neural networks have been developed in previous studies [13–15]. These studies have found that broader lateral projections can result in distinct pairwise correlation structures [15]. Furthermore, stability analysis of these models shows that the distance of projections has a critical effect on network stability: if inhibitory projections are broader than the excitatory projections, the fixed points of the network can become unstable [13], which can result in unreliable tracking of inputs [14]. These studies, however, have not examined the consequences of having cell types and assumed homogeneous inhibitory populations.

In cortical networks, diverse inhibitory subtypes including parvalbumin (PV), somatostatin (SST), and vasoactive intestinal polypeptide-expressing neurons (VIP) form circuits with excitatory (E) neurons with distinct connectivity statistics [10, 16, 17]. Several theoretical works have examined networks with heterogeneous inhibitory cell types. Wilson-Cowan-type models incorporating cell types have been used to study inhibitory stabilization and subtractive/divisive modulations [18] and to describe visual processing of objects superimposed on a background [19]. A rate-based circuit model has shown that PV and SST neurons may each be involved in encoding the mean and variance of predictions in prediction error neurons [20].

Recent work has studied the interplay between the inhibitory pathway from SST to E and the disinhibitory pathway involving PV, showing that SST can exhibit multiple gain modulations depending on the synaptic weights. [21]

These works have suggested the role of cell types in network computations, but did not address realistic, spatially-structured connectivity among different cell types and in particular did not address distance-dependent modulations.

Understanding how cell types and their specific distance-dependent connectivity influences neural computations is an important aspect of cortical processing

* To whom correspondence may be addressed. Email: soonhokim@gatech.edu or hannahch@gatech.edu

that is not well understood. The computational functions of inhibitory neurons can be understood through their arithmetic operations on neuronal input-output functions [22]. In the mouse primary visual cortex (V1), local and moderate activation of PV neurons results in divisive modulations on excitatory response curves to stimuli while the effect of SST neurons is subtractive [23–27]. However, recent evidence shows that when activated distally, SST neurons inhibit excitatory neurons receiving visual stimuli in a divisive manner while PV neurons exert subtractive modulations [28]. Anatomical data showed that SST neurons form broader axonal projections than PV neurons do [28–30]. Furthermore, a computational model of spiking neurons suggested that this long-range inhibition is necessary to reproduce the effects [28]. On the other hand, VIP neurons may increase the response gain, possibly through disinhibition [7, 31].

While spatially-embedded spiking neural networks of cortical populations incorporating cell types have recently been developed [28, 32], the nature of large spiking network models has limited these previous studies to simulation-based analyses, lacking theoretical insights. A systematic analysis of how position-dependent activation of PV, SST and VIP neurons modulates neural activity, therefore, is missing. A biologically-informed computational model of V1 enabling such analysis *in silico* would provide mechanistic insight into these experimental results. A mean-field model in particular can be tractable under some assumptions, allowing direct computation of important network features such as the eigenspectrum of the linearized dynamics. Furthermore, such models would provide a platform to understand the role of cell-type-specific structure in information processing across cortical networks.

Here we develop a mean-field model of spatially-extended spiking neural networks in V1. We first construct the model, incorporating distinct, cell-type-specific connectivity and derive conditions that achieve excitatory-inhibitory balance in the thermodynamic limit. We use an approach based on the Fokker-Planck equation to compute the position-dependent stationary firing rates of the model and validate them against spiking neural network simulations. We examine stability features of the network, specifically how long-range SST projections affect network stability. We further characterize the spatiotemporal features of the network dynamics across the stability boundary, finding significant differences in the heterogeneous network. Finally, we examine gain modulations during activation of specific inhibitory cell types by examining shifts in the stationary firing rates with input strength and find cell-type-specific and spatially-dependent effects. A linear response analysis suggests that shifts in the balance of excitation and inhibition through disexcitation or disinhibition may be a mechanism for the differential modulations.

II. RESULTS

A. Network Model with Inhibitory Cell Types

We construct a spatially-organized network of spiking neurons and incorporate cell-type-specific connectivity. The model consists of N neurons that are uniformly distributed on a 1-dimensional space with periodic boundary conditions, $\Gamma = (0, 1]$ (i.e., a ring). The network consists of $N_e = q_e N$ excitatory and $N - N_e$ inhibitory neurons which are subdivided into $N_p = q_p N$ PV, $N_s = q_s N$ SST, and $N_v = q_v N$ VIP neurons with $q_e + q_p + q_s + q_v = 1$. We set $q_e = 0.8$, $q_p = 0.1$, and $q_s = q_v = 0.05$, approximately following anatomical evidence [11] (see Figs. 1a, b for model schematics).

We first assume that the neurons follow leaky integrate-and-fire (LIF) dynamics with current-based synapses (see Eqs. 9, 10 in Sec. IV A). The probability with which the jth neuron of cell type β at position $y = j/N_\beta$ (where β takes on indices e, p, s, and v for E, PV, SST, and VIP neurons) connects to the kth neuron of type α at $x = k/N_\alpha$ is given by

$$k^{\Gamma}_{\alpha\beta}(x - y) = \bar{k}_{\alpha\beta} g(x - y; 0, \sigma_\beta). \tag{1}$$

Here $\bar{k}_{\alpha\beta}$ controls the overall connectivity probability from β to α (we use $\bar{\cdot}$ to denote the spatial average, i.e., $\bar{k}_{\alpha\beta} = \int_\Gamma k^{\Gamma}_{\alpha\beta}(x')dx'$). We select relative values to match recent anatomical data from layer 2/3 of V1 in mice [17] (Fig. 1c; see also Table I in Methods). Additionally, we scale all probabilities so that the overall connectivity of the network is 1%, imposing sparse connectivity. The distance-dependence is given by the wrapped Gaussian function $g(x - y; 0, \sigma_\beta)$, where σ_β is the characteristic projection distance of β-type neurons (see Methods A). The values for σ_β are also chosen based on recent anatomical evidence; motivated by the experimental evidence of broad SST axonal projections and more local PV and VIP projections [28–30, 33], we set $\sigma_s = 0.2$ and $\sigma_p = \sigma_v = 0.1$ (Fig 1d). Excitatory projections are set to $\sigma_e = 0.1$ unless stated otherwise. If a synapse is formed from a presynaptic neuron of type β to a postsynaptic one of type α, the weight of the synapse is given by $J_{\alpha\beta}$, where the synaptic weight matrix J is tuned to achieve a balanced state as outlined below.

B. Derivation of balanced solution in the thermodynamic limit

The kth neuron of cell type α receives inputs $I_{\alpha,k}$ given by a sum of recurrent synaptic inputs, described above, and a cell-type- and position-dependent external current $F_\alpha(x)$. We consider a case where $F_\alpha(x)$ have Gaussian spatial profiles. The external input to population α is given by a weighted sum of a constant term and spatially structured term, $F_\alpha(x) = \bar{F}_\alpha[(1 - p_\alpha) + p_\alpha g(x; x_f, \sigma_{\alpha f})]$, where the stimulus is centered at $x_f = 0.5$ and has a

broadness given by $\sigma_{\alpha f} = 0.25$. The relative weight of the spatially-structured input is given by p_α, and $\bar{F}_\alpha = \int_\Gamma F_\alpha(x)dx$ is the mean current input to population α. Following studies of networks with E-I balance [8, 13], we assume that the synaptic weights follow scaling $J_{\alpha\beta} = j_{\alpha\beta}/\sqrt{N}$ and inputs follow $F_\alpha = f_\alpha\sqrt{N}$ with network size N, where $j_{\alpha\beta}$ and f_α do not depend on N. We assume that other parameters, such as the threshold and reset potentials, do not depend on N. Under these assumptions, a neuron receives $O(N)$ excitatory inputs but requires $O(\sqrt{N})$ presynaptic neurons to activate during an integration window to produce a spike [34]. In order for a stable stationary firing rate solution to exist, a dynamic balance between excitation and inhibition must be maintained [8, 13, 35].

The kth neuron of type α (at position $x = k/N_\alpha$) has mean firing rate $\nu_\alpha(x) = \langle E[s_{\alpha,k}]\rangle$, where $E[\cdot]$ denotes the average over network configurations, $\langle\cdot\rangle$ the time average, and $s_{\alpha,k} = \sum_{t'_{\alpha,k}} \delta(t - t'_{\alpha,k})$ is the spike train of

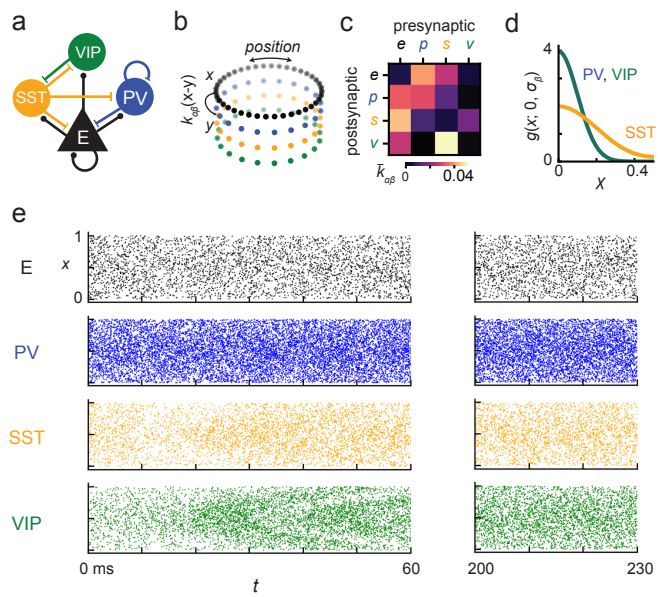

FIG. 1. Model schematic and spiking dynamics. (a) The cortical network model consists of excitatory (E) neurons and PV, SST, and VIP inhibitory neurons. The schematic shows the major projections within and between cell types. (b) Cartoon of the spatial structure of the network. Neurons are placed with even spacing in a ring configuration. The probability of connection depends on the relative position $x - y$ between the position of the presynaptic and postsynaptic neurons. (c) Cell-type-specific connectivity probabilities. Brighter color represents a greater probability that the corresponding presynaptic cell type will project to the postsynaptic cell type. Indices e, p, s, and v correspond to E, PV, SST, and VIP neurons, respectively. (d) Spatial projection kernel of each inhibitory cell type. (e) Raster plot of example spiking neural network run with a network size of $N = 5 \times 10^5$. The vertical axes represents the position and the horizontal axes the time of the spike.

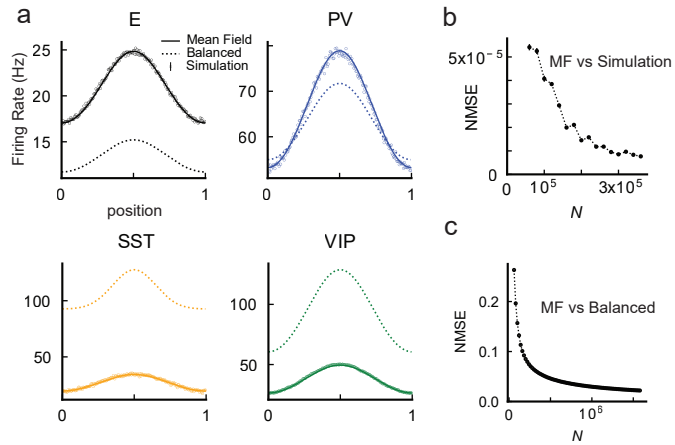

FIG. 2. Firing rates in the four-population (E, PV, SST, and VIP) model. (a) Stationary firing rate from mean-field theory (solid lines), analytical solutions in the thermodynamic limit (dashed lines), and firing rates calculated from simulations (error bars) from spiking networks with $N = 3 \times 10^5$. For simulations, each data point represents the mean firing rate of neurons within a window of size 0.05; error bars correspond to mean $\pm$ sem over 10 independent network initializations. (b) Normalized mean square error (NMSE) between mean-field theory and simulated firing rates as a function of network size N. (c) NMSE between the mean-field model with varied network sizes and the balanced solution in the thermodynamic limit.

the neuron. The mean input current is given by

$$\begin{aligned}\mu_\alpha(x) &\equiv \langle E[I_{\alpha,k}(t)]\rangle \\ &= \sqrt{N}\left[\sum_\beta (w_{\alpha\beta} * \nu_\beta)(x) + f_\alpha(x)\right] \end{aligned} \tag{2}$$

where $w_{\alpha\beta}(x') \equiv q_\beta j_{\alpha\beta} k^\Gamma_{\alpha\beta}(x')$ and "$*$" indicates circular convolution, i.e., $(w_{\alpha\beta} * \nu_\beta)(x) = \int_\Gamma w_{\alpha\beta}(x')\nu_\beta(x - x')dx'$. The balanced state exists when the mean input currents obey $O(1/\sqrt{N})$ scaling,

$$\sum_\beta (w_{\alpha\beta} * \nu_\beta)(x) + f_\alpha(x) = O(1/\sqrt{N}). \tag{3}$$

Taking $N \to \infty$ (which we call the thermodynamic limit) gives a Fredholm equation of the first kind, which in the Fourier domain becomes

$$\sum_\beta \tilde{w}_{\alpha\beta}(n)\tilde{\nu}_\beta(n) + \tilde{f}_\alpha(n) = 0 \tag{4}$$

where the tilde indicates a Fourier transform, i.e. $\tilde{h}(n) \equiv \int_\Gamma e^{-2\pi x n i} h(x)dx$, and n is the Fourier mode. The solution is given by

$$\tilde{\nu}_\alpha(n) = \frac{\sum_\beta \tilde{f}_\beta \tilde{A}_{\alpha\beta}}{\det(\tilde{W})} \tag{5}$$

where $\tilde{W}$ is a matrix whose elements are $\tilde{w}_{\alpha\beta}$ and $A_{\alpha\beta}$ are cofactors of $\tilde{W}$. Eq. 5 must hold for every n for which $\det \tilde{W} \neq 0$. If the determinant equals 0 at some Fourier mode, then for a solution to exist, $\sum_\beta \tilde{f}_\beta \tilde{A}_{\alpha\beta}$ must also equal zero at that Fourier mode.

The solutions are viable only if $\tilde{\nu}_\alpha$ has a well-defined inverse Fourier transform, such that

$$\lim_{n\to\infty} \tilde{\nu}_\alpha(n) = 0$$

for each $\alpha = e, p, s, v$. Each term $(w_{\alpha\beta} * \nu_\beta)(x)$ in Eq. 2 is a convolution of two Gaussian functions, which is itself a Gaussian with spatial variance equal to the sum of those of $w_{\alpha\beta}$ and ν_β. This implies that the external current inputs to each population α must be broader than the recurrent projections of every other population β (i.e., $\sigma_\beta < \sigma_{\alpha f}\ \forall \alpha, \beta$) to satisfy Eq. 4 [13]. Under these conditions, the stationary firing rates can be derived by taking the inverse Fourier transform of Eq. 5 to get (see Sec. IV C for details)

$$\nu_\alpha(x) = \bar{\nu}^f_\alpha + \sum_\beta \bar{\nu}^g_{\alpha\beta} g\left(x; 0, \sqrt{\sigma^2_{\beta f} - \sigma^2_\alpha}\right), \qquad (6)$$

where $\bar{\nu}^f_\alpha$ and $\bar{\nu}^g_{\alpha\beta}$ are defined in Eqs. 19-21.

If each input has the same profile, i.e. $\sigma_{\beta f} = \sigma_f$ and $p_\alpha = p$, Eq. 6 simplifies to

$$\nu_\alpha(x) = (1-p)\bar{\nu}_\alpha + p\bar{\nu}_\alpha g\left(x; x_f, \sqrt{\sigma^2_f - \sigma^2_\alpha}\right), \qquad (7)$$

where $\bar{\nu}_\alpha$ is the spatial mean of the firing rate. Synaptic weights $j_{\alpha\beta}$ and input values $\bar{f}_\alpha$ that achieve network balance can be generated through numerical means (see Sec. IV C and Table II). Spiking neural network simulations using balanced parameters are shown in Fig. 1e.

C. Finite-N solutions

Under mean-field assumptions, firing rates for networks of finite size N can be approximated with a semi-analytic approach. The current input $I_{\alpha,k}$ is replaced by a diffusion term $\mu_\alpha(x) + \sqrt{2D_\alpha(x)}\xi(t)$ where $\mu_\alpha(x)$ is the mean and $D_\alpha(x)$ the variance of the input to neurons of type α, and $\xi(t)$ is a zero-mean white noise. Given $\mu_\alpha(x)$ and $D_\alpha(x)$, the stationary firing rates $\nu_\alpha(x)$ can be computed by numerically integrating the Fokker-Planck equation as introduced in previous works [36, 37]. Since $\mu_\alpha(x)$ and $D_\alpha(x)$ themselves depend on $\nu_\alpha(x)$, this forms self-consistent equations from which an iterative approach can be used to numerically compute the stationary firing rates (details in Sec. IV B).

Comparison of the stationary firing rates with LIF network simulations shows that the mean-field description accurately predicts the stationary firing rates (Fig. 2a). The normalized mean square error (NMSE) between the mean-field fixed points and rates computed from simulations decreases with network size (Fig. 2b). Furthermore, we see that as N increases the network converges to the analytical solutions satisfying the balanced state in the thermodynamic limit in Eq. 7 (Fig. 2c).

D. Stability Analysis

One of the key features we include in the model is the long-range projections of SST neurons, i.e. $\sigma_s > \sigma_p, \sigma_v$. This is based on anatomical evidence as well as fact that long-range SST projections are necessary in spiking neural network models to reproduce the divisive effects of lateral inhibition by distal SST neurons [28]. However, previous work
on spatially distributed E-I networks with a single type of inhibitory population showed that inhibitory projections must be strictly shorter than excitatory projections ($\sigma_i < \sigma_e$) to maintain a stable balanced state [13, 14]. Here we examine whether long-range SST projections in a network composed of different inhibitory subtypes cause instability in our proposed model.

To do this, we linearize the firing rate dynamics about the fixed point,

$$\tau \frac{\partial \nu_\alpha}{\partial t} = -\nu_\alpha + \gamma \mu_\alpha \Theta(\mu_\alpha). \qquad (8)$$

where τ is the characteristic time scale of the network, $\gamma = 1$ is the gain of the neuron, and Θ is the Heaviside step function. This approximates the network dynamics as threshold linear, which is accurate for high inputs [13, 35, 38, 39]. Eq. 8 thus describes the position-dependent linearized dynamics about the fixed point. We note that although the fixed point will depend on the static inputs $\bar{f}_\alpha$, its stability will not depend on $\bar{f}_\alpha$ as long as the fixed point is strictly positive. Under this approximation, the fixed point is stable whenever the matrix $C(n) = \tilde{W} - \epsilon I$ (where $\epsilon = (\gamma\sqrt{N})^{-1}$ and I is the identity matrix) has eigenvalues λ_n with negative real parts $\mathrm{Re}(\lambda_n)$ for each Fourier mode n.

We first consider the stability of a network of size $N = 3 \times 10^5$ with a homogeneous inhibitory neuron population by setting $q_i \equiv q_p = 0.2$ and $q_s = q_v = 0$. This is similar to the model in Ref. [13], but with inhibitory neuron parameters specifically derived from PV neurons. We computed the maximum real part of the eigenvalues for varying excitatory and inhibitory projection range σ_e and σ_i (Fig. 3a, top panel). The dashed line indicates the boundary between stable and unstable networks. When $\sigma_e = 0.05$ and $\sigma_i = 0.2$ (purple asterisk on Fig. 3a), the network lies in the unstable region. We then considered the stability diagram of the network with heterogeneous inhibitory neurons and vary σ_s along with σ_e while keeping $\sigma_p = \sigma_v = 0.1$ (Fig 3a, bottom panel). The boundary of stability has a significantly different profile. When $\sigma_s = 0.2$ and $\sigma_e = 0.05$ (black asterisk on Fig. 3a), stability is maintained.

Increasing N for both networks increases the range of instability (Fig. 3b). For the homogeneous model, the

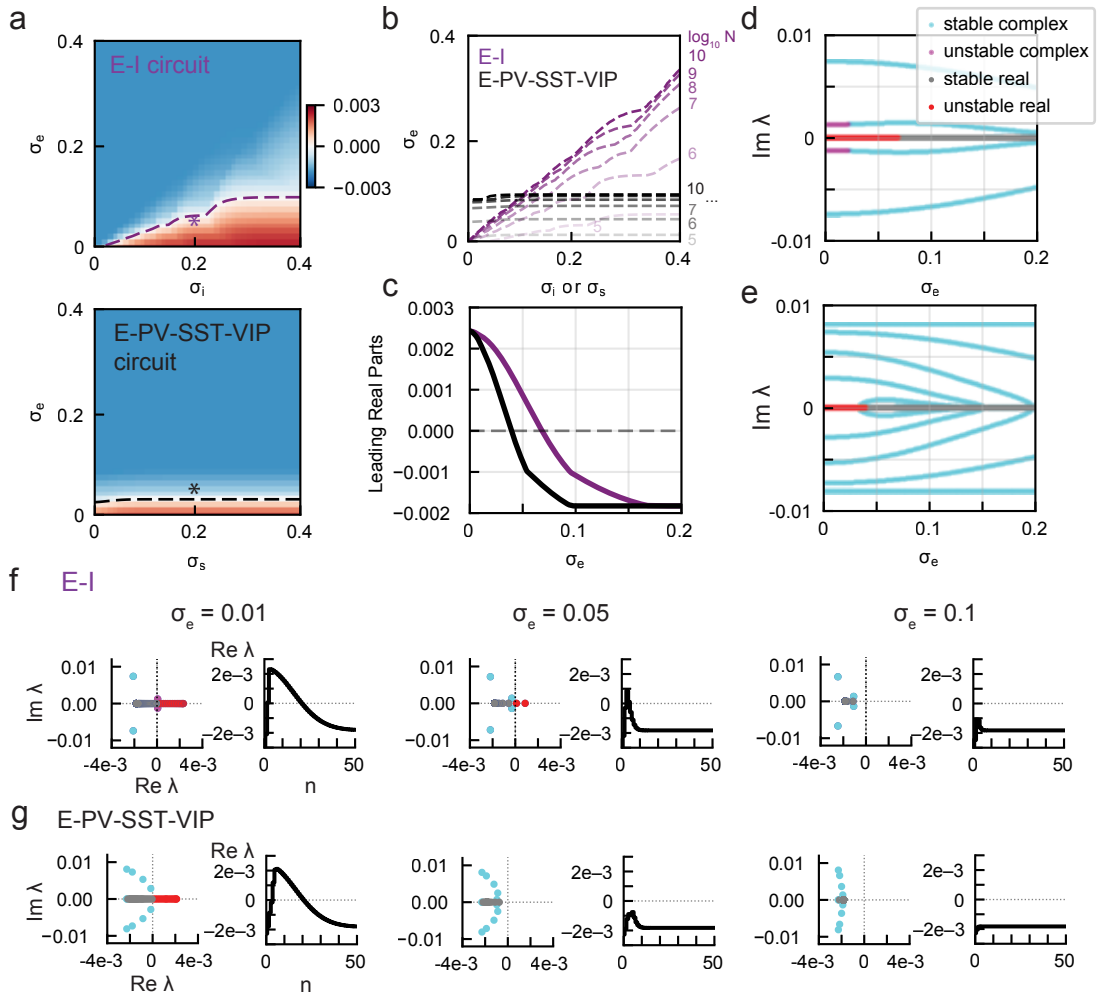

FIG. 3. Stability in networks with homogeneous and heterogeneous inhibitory neuronal populations. (a) Stability diagrams of an E-I circuit with a homogeneous inhibitory neuron population consisting of PV neurons only (top) and of the E-PV-SST-VIP circuit with heterogenous inhibitory neurons (bottom; $N = 3 \times 10^5$). The color indicates the maximum value of $\mathrm{Re}(\lambda_n)$ for the corresponding inhibitory projection distance σ_i and excitatory projection distance σ_e. Red indicates positive eigenvalues (unstable) and blue negative values (stable). The dashed lines trace the borders of stability. (b) Stability boundaries for E-I (purple dashed lines) and E-PV-SST-VIP circuits (black dashed lines) for varying network sizes N (from 10^5 to 10^{10}, with darker shades indicating higher N). (c) Leading real eigenvalue part for varying σ_e for the two circuits. $\sigma_i = 0.2$ for the homogeneous circuit (purple) and $\sigma_s = 0.2$ for the heterogeneous circuit (black). (d) Imaginary parts of eigenvalues for varying σ_e in the homogeneous circuit. Pure real eigenvalues are colored gray (stable) and red (unstable) while complex eigenvalues are cyan (stable) and purple (unstable). (e) Same as (d) for the heterogeneous circuit. (f) Eigenspectrum λ_n for the homogeneous E-I circuit for $\sigma_e = 0.01$ (left panel), $\sigma_e = 0.05$ (center), and $\sigma_e = 0.1$ (right). In each panel, the left plot show the eigenspectrum on the complex plane with the same color coding as in (d-e). The right plots show the real part of the eigenvalue for varying Fourier component n. (g) Same as (f) for the E-PV-SST-VIP circuit.

stability-instability boundary trends towards the diagonal line $\sigma_e = \sigma_i$. This indicates that as $N \to \infty$, the network is unstable as long as $\sigma_i > \sigma_e$. However, for the heterogeneous network the boundary converges to a horizontal line, and a region exists for which the network remains stable when $\sigma_s > \sigma_e$. Network stability is thus insensitive to the broadness of SST projections. In contrast, the broadness of PV projections in the heterogeneous network causes instability even when SST and VIP neurons are kept short-range (see Supplemental Material, Fig. S1), indicating that projections from PV neurons specifically are crucial in maintaining dynamical stability of the network. Cell-type-specific connectivity underlies this effect, and in particular PV self-inhibition is necessary for its stabilizing role, as demonstrated by a decomposition analysis in the Supplemental Material, Sec. 1.

The E-PV-SST-VIP circuit hence has a larger region of dynamical stability. This is seen explicitly in Fig. 4c, which displays the real parts of the eigenvalue when in-

hibitory projections are fixed and σ_e varied. Instability occurs when σ_e is below 0.07 for the homogeneous model and below 0.04 for the heterogeneous model (Fig. 3c). The two models show distinct imaginary components, as seen in Figs. 3d, e. Furthermore, in both the homogeneous and heterogeneous model, the first emergent unstable eigenvalues are pure real (red line). The homogeneous model additionally displays unstable complex eigenvalues at very narrow σ_e.

To further characterize the bifurcation, eigenspectra of $C(n)$ are shown for three values of σ_e in Fig. 3f (E-I circuit) and Fig. 3g (E-PV-SST-VIP circuit). Each pair of panels show the eigenspectrum on the complex plane on the left and the real eigenvalue parts for varying Fourier node n. In both models, the critical Fourier node n^c that initially becomes unstable (Re $\lambda(n^c) \geq 0$) is strictly positive, indicating a Turing bifurcation.

E. Spatiotemporal features of network dynamics

We then proceeded to verify the spectral analysis of the mean-field model in Fig. 3 with spiking neural network simulations. Spatially-organized rastor plots, shown in Fig. 4a for the E-I circuit, show the emergence of spatial patterns for $\sigma_e = 0.01$ and 0.05; when $\sigma_e = 0.1$, the firing pattern reflects the smooth Gaussian input. The same is seen for the E-PV-SST-VIP circuit in Fig. 4b, but with different spatial frequencies.

We quantified the temporal variance of firing rates of the two models for varying σ_e in Fig. 4c. As predicted by the transition points in Fig. 3c, temporal variance increases rapidly as σ_e is reduced beyond a certain value that is approximately at the critical σ_e predicted from the stability analysis (dotted vertical lines, Fig. 4c), which is higher for the E-I circuit compared to the E-PV-SST-VIP circuit.

We further examined the emergent spatial patterns in the models. Fig. 4d displays the peak spatial frequency in the two models. When σ_e is very high (> 0.05), both circuits track the spatial frequency of the Gaussian input with a frequency of 1 cycle per spatial unit. Spatial patterns emerge in both models as σ_e is decreased. In the unstable region, we expect the Fourier nodes n with unstable eigenvalues to strongly influence the spatial frequency of the resulting dynamics. We thus compared the spatial patterns in simulations against the peak unstable Fourier modes n^* (peaks of black lines in Figs. 3f, g) represented by open circles in Fig. 4d. For very small $\sigma_e < 0.03$, the peak spatial frequencies observed in simulations closely match n^* in both models. In the intermediate range between 0.03 and 0.06 around the bifurcation points, there is a competition between the frequency of the Gaussian input and the dominant Fourier mode, and the peak spatial frequency has an intermediate value.

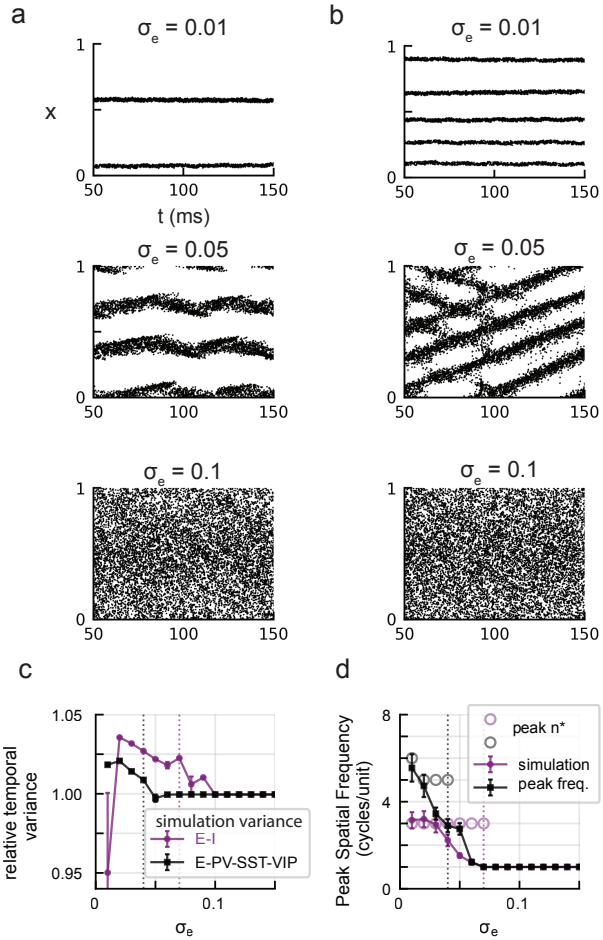

FIG. 4. Spatiotemporal network activity in spiking network simulations. (a) Raster plot of excitatory neurons in the E-I circuit for $\sigma_e = 0.01$ (top), 0.05 (middle), and 0.1 (bottom) in response to Gaussian input. For visibility, only spikes from one in every eight neurons is shown. (b) Same as (a) for the E-PV-SST-VIP circuit. (c) Mean relative temporal variance of firing rates for E neurons in the two circuits, for varying σ_e. Raw variance is normalized against the variance when $\sigma_i = 0.2$. Shown are the mean $\pm$ sem over 20 independent simulations. Vertical dotted lines show the bifurcation points from Fig. 3a. $\sigma_i = 0.2$ for the E-I model and $\sigma_s = 0.2$ for the E-PV-SST-VIP model. (d) Peak spatial frequency from simulations (purple dots for E-I, black dots for E-PV-SST-VIP) of firing rate activity in the two models for varying σ_e. Open circles indicate the peak unstable frequency n^* from mean-field theory.

F. Cell-type-specific gain modulations

Next, we examined the gain modulations induced by stimulating specific cell types in the mean-field model. We define gain modulations as changes in the slope of the visual response curves in excitatory neurons: a decrease in the slope indicates a divisive modulation, while a vertical shift without slope change indicates a purely subtractive modulation [22, 26, 28]. We presented a Gaussian-

shaped input current to excitatory and PV neurons centered at $x_v = 0.5$ with varying intensities to simulate visual inputs of different contrast levels. Cell-type-specific modulatory signals activating inhibitory neurons were induced with an additional Gaussian-shaped input current centered at x_C which was either proximal ($x_C = 0.5$) or distal ($x_C = 0$) to the site of the visual stimulus input (Fig. 5a; details in Sec. IV F). The spatial structure of the E response with PV (blue), SST (gold) and no stimulation (black) showed distinct shapes with proximal stimulations (Fig. 5b, left). However, the slope of excitatory responses to varying stimulus intensity did not decrease when paired with stimulation of any types of inhibitory neurons, i.e. no divisive gain changes were observed (Fig. 5b, right). Different spatial response profiles were also observed with distal stimulation of inhibitory subtypes, but again, with no divisive modulations (Fig. 5c).

Experimental evidence suggests that both PV and SST neurons can exert divisive gain modulations (i.e., negative slope changes) depending on the stimulation conditions and the location of their stimulation relative to the site of visual input [23–25, 28]. We reasoned that the lack of divisive gain modulations in the model may be due to simplifications in the model, in particular due to the current-based synapses assumed in the model. This is manifested in the balanced solution Eq. 5, which is linear in external inputs $\tilde{f}_\beta$. We thus incorporated conductance-based synapses into the model; mean-field firing rates can be computed with a similar approach to the current-based case with modified parameters and a voltage-dependent diffusion term (see Sec. IV D). We first verified that the mean-field results with the conductance-based synapses agreed with the corresponding spiking network simulations (see Supplemental Material, SFig. 2). We repeated the stability analysis across spatial scales of excitatory and inhibitory projections to account for voltage-dependent synaptic transmissions and found similar results to the current-based model (Supplemental Material, SFig. 3).

Having verified that the conductance-based mean-field model generates the same results on spatial response profiles and projection-dependent stability as with the current-based synapses model, we next simulated proximal and distal activations of inhibitory neurons using the mean-field model with conductance-based synapses. When proximal stimulation was given to the conductance-based network, again distinct profiles emerged—PV and SST stimulation completely suppressed excitatory responses at the site of visual input, while VIP stimulation exerted a subtractive effect (Fig. 5d). With distal stimulation, the spatial profile of the excitatory response sharpened with PV stimulation. In addition, distal PV stimulation caused a subtractive effect on the E response to visual input strengths (no slope change), while distal SST stimulation caused a divisive gain change (decrease in slope). Distal VIP stimulation caused slight multiplicative gain change (increase in slope, Fig. 5e). These distance- and cell-type dependent modulations are consistent with experimentally observed effects of both proximal and distal PV or SST stimulation in mouse V1: both resulted in strong divisive gain modulations in excitatory neurons when the activation of the inhibitory population was proximal, and only SST activation resulted in divisive operations when distal [28]. The positive gain change induced by VIP neurons is also consistent with a previous experimental study [31].

G. Direct inhibition promotes divisive gain modulations

Inhibitory neurons can exert gain modulations through multiple pathways [21]. Here we examine whether the direct inhibition or indirect disexcitation may underlie the distinct modulatory effects. Similar to the network response, the slope of an input-output curve of a single neuron can be interpreted as neuronal gain [22]. It is known that the background synaptic input affects the gain of a neuron's response [40]. We can thus trace the gain modulation of the network to shifts in the background inputs of neurons due to cell-type-specific activations. Distal SST neurons, due to their long-range projections, can directly inhibit E neurons in the visual field of stimuli. On the other hand, distal PV neurons primarily act on E neurons in the visual field polysynaptically by inhibiting presynaptic E neurons, thereby decreasing excitation (Fig. 5f). Within the mean-field framework, linear response theory can be used to measure the precise response of neurons to perturbations in the input, giving us a precise way to measure neuronal gain.

We used linear response theory to quantify the neuronal gain of excitatory neurons in the network at the center of the visual input. Specifically, we examined how the gain changed when direct inhibition was increased (simulating the distal SST effects) versus when the background excitatory input was decreased (simulating the distal PV effects). A frequency-dependent perturbation was introduced to the visual input in the two cases as well as to the unmodified control (details in Sec. IV G). Inhibition was increased and excitation decreased each up to 10-fold, with results summarized in Supplemental Material, SFig. 4. Here we examined the amplitude and angle of the response with a 2-fold increased inhibition and 10-fold decreased excitation, and compared them to the base case (Fig. 5g). The amplitude of the response in the control case showed a peak at 10 Hz, indicating a resonant frequency, and there was an associated positive phase shift (black curve, Fig. 5g). When excitation was decreased, the response was similar to the control case, exhibiting the same resonant frequency and phase shift (cyan curve). However, when inhibition was increased, the amplitude of the response was shifted downward, indicating a lower gain (purple curve). Moreover, the resonant frequency disappeared with increased inhibition. These results indicate that increased inhibition induces a negative gain change in the excitatory neurons across

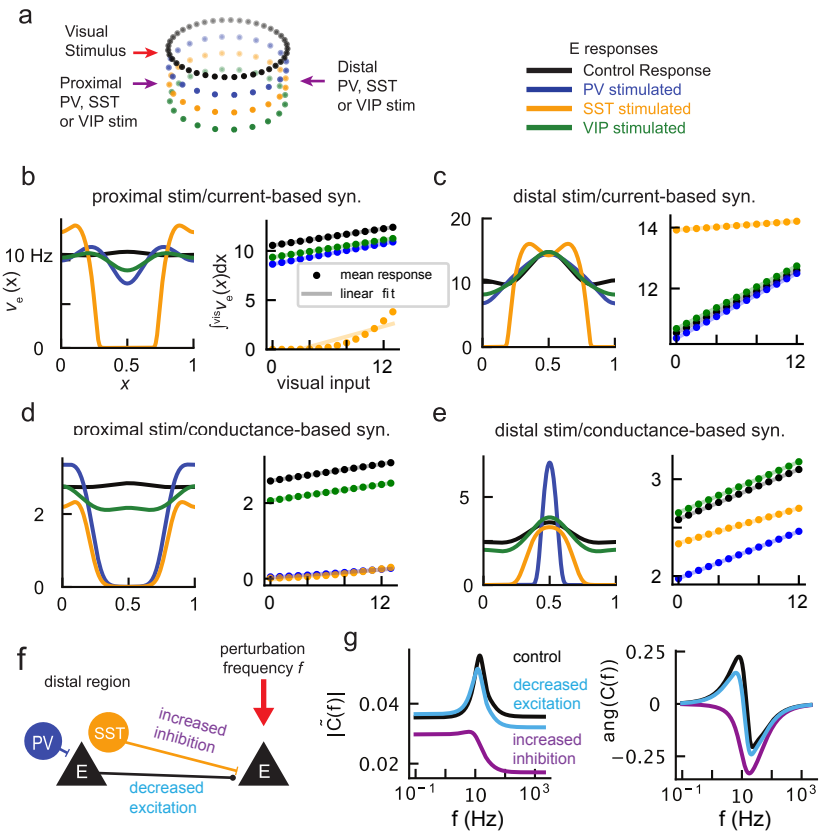

FIG. 5. Cell-type-specific gain modulations. (a) Schematic of stimulations. Visual stimulus is given as input to E and PV neurons centered at $x_v = 0.5$. For proximal modulations, PV, SST, or VIP neurons at $x_v = 0.5$ were stimulated. For distal modulations, neurons at $x_C = 0$ were stimulated. (b) Left: Response profiles of E neurons in the current-based model with PV (blue), SST (gold), VIP (green) proximal stimulation and without activation of inhibitory neurons (black). Right: Dots represent E responses averaged across the region of visual input for varying input strength (see Eq. 29). Shaded lines show linear fits. (c) Same as (b) but for distal PV, SST, and VIP stimulation. (d, e) Same as (b, c) but with the conductance-based model. (f) Schematic of linear response analysis. Oscillatory perturbation is applied to the visual input. The linear response with increased long-range inhibition (purple) and decreased long-range excitation (cyan) are computed and compared against the unaltered network conditions (black). (g) Linear response amplitude (left) and phase shift (right).

all stimulus frequencies, which may act as a mechanism for divisive effects of distal SST stimulation. Distal PV stimulation decreases excitation without increasing direct inhibition, resulting in a subtractive effect. Meanwhile, a strong local stimulation of either PV or SST can induce divisive operations through direct inhibition.

III. DISCUSSION

We derived mean-field equations for a spatially-organized spiking neural network with excitatory and three inhibitory sub-populations. The neurons have distance-dependent connectivity rules that depend on pre- and post-synaptic cell types, informed by anatomical data from mouse primary visual cortex. Given the cell-type specific connectivity, we derived conditions for E-I balance in the network. The model revealed dynamical properties conferred by inhibitory heterogeneity that may indicate computational benefits. The heterogeneous network maintained stable dynamics even with long-range SST inhibition; this was in contrast to the network with homogeneous inhibitory neurons, whose projections were restricted to be shorter than those of excitatory neurons in order to maintain stability as suggested by a previous theoretical study [13]. Thus, our result, by introducing inhibitory subtypes, closes the gap between the previous theoretical prediction where inhibitory projections are restricted to be local [13] and contradictory experimental observations of long-range inhibition [28–30]. Furthermore, activation of each inhibitory cell type performed distinct modulations on excitatory neurons processing visual input, in agreement with recent experimental observations [25, 28, 31]. This demonstrates that there are multiple modes of computations that can be activated flexibly depending on spatial relation between inhibitory modulatory signals and visual stimuli.

Our work sheds light on the computational role of neu-

ronal cell type diversity and their distinct spatial connectivity in the cortex. The balance of excitation and inhibition in the cortex is believed to be the basis for irregular spiking activity and heterogeneity of responses [8]. By extending previous work on spatially-distributed E-I networks [13, 15], we demonstrated that the network composed of excitatory and three main subtypes of inhibitory neurons—PV, SST, and VIP—can achieve balance to each of its populations. Our analytical findings give us a simple description to determine balance in a multi-population network depending on connectivity and synaptic weights. Understanding how balanced states can be altered by changes in connectivity may be important in understanding network activity in neurological disorders [41–43].

Our mean-field approach further allowed us to directly compute the eigenspectrum of the network's fixed state. Our model shows that neural heterogeneity enhances network stability, allowing stable firing rate readouts even in the presence of long-range inhibition. In contrast, networks with a homogeneous inhibitory population displayed unstable dynamics and high response variability with long-range inhibition. This result thus implicates possible computational advantages of cell type diversity. Loss of stability was caused by Turing bifurcations in both heterogeneous and homogeneous models. Simulations confirmed the emergence of spatial patterns as excitatory projections became local, with a higher spatial frequency exhibited in the heterogeneous model.

Identifying neuronal cell types and their functional roles has emerged as a major problem in neuroscience [17, 44, 45]. Computational studies have played an indispensable role in understanding the role of inhibitory neuron subtypes in dynamics and computations [18–20, 32, 46–48]. Our work complements these studies by providing additional mechanisms by which networks may perform divisive and subtractive computations. For example, Wilmes et al. [20] showed that divisive and subtractive operations on excitatory rates by PV and SST neurons, respectively, may account for computations needed to encode the variance and mean of a variable. Recent theoretical work by Bos et al. analyzed the multiple pathways through which SST modulate E neurons and showed that SST activation can exert differential gain modulations on excitatory neurons depending on the synaptic weights [21]. Our work complements these studies by showing that PV and SST neurons can perform various degrees of divisive or subtractive modulations depending on the distance between their activation and the stimulus input sites. Thus, inhibitory neurons, by utilizing their heterogeneous projection patterns across the cortical network, may perform a range of distinct operations on spatially organized stimuli in an effective and robust manner. The linear response analysis suggest that a shift in the balance of excitation and inhibition may underlie divisive gain changes, with direct inhibition contributing to divisiveness.

Our results highlight the computational benefits of a heterogeneous neuronal population in recurrent neural networks. A recent line of work has found that the degree of heterogeneity within a cell type can play a major role in network computations [47, 48]. While our work focused on heterogeneity in intrinsic properties and projection patterns across cell types and assumed no variation in parameters within each cell type, it would be interesting to investigate the interaction of within- and between-population heterogeneity. In another work, Winston et al. found that heterogeneous cell types emerge when training spiking neural networks to perform temporal processing tasks [46]. It is an open question whether PV, SST, and VIP-like structures may emerge from network optimization under certain objective functions and constraints.

The current work can be expanded in several ways. One line of study would be to investigate how the network can take computational advantage of the response properties explored here by employing them in visual processing tasks. In addition, further biophysical details neglected in the present model, such as dendritic integration [28], can be incorporated to make the mean-field model more realistic.

IV. METHODS

A. Neuronal dynamics and spatial projections

The membrane potential $V_{\alpha,k}$ of the kth neuron of type α ($= e$, p, s, or v) is given by leaky integrate-and-fire (LIF) equations

$$\tau_\alpha \frac{dV_{\alpha,k}}{dt} = g_{L,\alpha}(E_L - V_{\alpha,k}) + I_{\alpha,k}(t), \tag{9}$$

where τ_α is the membrane time constant, set to 30 ms for $\alpha = e$ and 20 ms otherwise; $g_{L,\alpha}$ is the leak conductance, set uniformly to 1 (dimensionless units); E_L is the leak reversal potential at 0; and $I_{\alpha,k}(t)$ is the input current, given by

$$I_{\alpha,k}(t) = \sum_{\beta\in\{e,p,s,v\}} \sum_{j=1}^{q_\beta N} J^{k,j}_{\alpha\beta} s_{\beta,j}(t) + F_\alpha(x). \tag{10}$$

Here $J^{k,j}_{\alpha\beta}$ is the synaptic weight from presynaptic neuron j of type β, $s_{\beta,j}(t) = \sum_{i'} \delta(t - t^{i'}_{\beta,j})$ is its spike train, $x = k/N_\alpha$ is the position of the kth neuron, and $F_\alpha(x)$ is a static, position-dependent external input. The membrane potential variable V and voltage-related parameters are given in dimensionless units.

When the membrane potential reaches the threshold $V_{\rm th}$, a spike is emitted and $V_{\alpha,k}$ is reset to the reset voltage $V_{\rm re}$ on the next time step. We set $V_{\rm th} = 1$ and $V_{\rm re} = 0$; numerical integration is performed using the Euler method with time step $\Delta t = 0.1$ ms

TABLE I. Cell-type-specific connectivity probabilities $\bar{k}_{\alpha\beta}$ used in the model.

		presynaptic cell type β			
		E	PV	SST	VIP
postsynaptic	E	0.06	0.35	0.23	0.05
cell type	PV	0.42	0.39	0.18	0.02
α	SST	0.35	0.09	0.05	0.14
	VIP	0.16	0.00	0.30	0.01

The synaptic weight $J^{k,j}_{\alpha\beta}$ from neuron j of cell type β (at position y) to neuron k of cell type α (at position x) is given by

$$J^{k,j}_{\alpha\beta} = \begin{cases} J_{\alpha\beta}, & \text{with probability } k^{\Gamma}_{\alpha\beta}(x-y), \\ 0, & \text{otherwise.} \end{cases} \tag{11}$$

Here $k^{\Gamma}_{\alpha\beta}(x-y)$ is the distance-dependent connectivity kernel.

The synaptic weight $J_{\alpha\beta}$ is assumed to scale with the network size as $J_{\alpha\beta} = j_{\alpha\beta}/\sqrt{N}$ where $j_{\alpha\beta}$ is a constant independent of N. External inputs scale according to $F_\alpha(x) = \sqrt{N} f_\alpha(x)$, while other parameters are constant with respect to network size.

We assume that the connectivity kernel is a wrapped Gaussian projection kernel with a broadness that depends on the presynaptic neuron type, i.e., $k^{\Gamma}_{\alpha\beta}(x-y) = g(x-y; 0, \sigma_\beta)$, where the wrapped Gaussian g is given by

$$g(x;\mu,\sigma) = \frac{1}{\sqrt{2\pi}\sigma} \sum_{n=-\infty}^{\infty} e^{-(x+n-\mu)^2/2\sigma^2}. \tag{12}$$

Gaussian spatial connectivity profiles have been used to fit anatomical data of rodent and cat cortex [17, 49, 50]. The Gaussian model breaks down for long-range connections beyond approximately 1 mm [51] which is beyond the range considered in the model. The assumption that the spatial connectivity kernel only depends on the cell type of the presynaptic neuron is a simplification based on evidence that the primary constraint on distance-dependent connectivity is the axonal projections of the presynaptic neurons [52, 53]. We note however that this assumption is not strictly necessary. Current inputs are given by

$$f_\alpha(x) = p_\alpha \bar{f}_\alpha g(x; x_f, \sigma_{\alpha f}) + (1-p_\alpha)\bar{f}_\alpha. \tag{13}$$

Here $\bar{f}_\alpha$ is the mean input to cells of type α and p_α determines the proportion of the input spatially localized at x_f.

B. Mean-field equations in the continuum limit

In the mean-field model, we take the continuum limit

$$\tau_\alpha \frac{dV_\alpha}{dt}(x) = g_{L,\alpha}(E_L - V_\alpha(x)) + I_\alpha(x,t) \tag{14}$$

TABLE II. Synaptic weights $j_{\alpha\beta}$ and external current input parameters $\bar{f}_\alpha = \bar{F}_\alpha/\sqrt{N}$ and p_α (see Eq. 13) used in Figs. 1-4. Values of $j_{\alpha\beta}$ and $\bar{f}_\alpha$ were chosen to achieve balance in the thermodynamic limit as described in the Methods.

		presynaptic cell type β				external	
		E	PV	SST	VIP	$\bar{f}_\alpha$	p_α
postsynaptic	E	0.76	0.92	0.20	2.00	2.6×10^{-4}	0.25
cell type	PV	0.83	1.71	0.20	1.49	6.0×10^{-5}	0.25
α	SST	0.20	1.95	2.00	0.20	1.3×10^{-4}	0.2
	VIP	0.32	1.19	0.32	2.00	1×10^{-5}	0.2

where the input current from Eq. 9 is replaced by a position-dependent effective field, modeled as a random process $I_\alpha(x,t) = \mu_\alpha(x) + \sqrt{2D_\alpha(x)}\xi(t)$. Here $\mu_\alpha(x)$ is the mean input current, given by a sum of recurrent inputs and position-dependent current input f_α (see Eq. 2),

$$\begin{aligned} D_\alpha(x) \approx & \frac{1}{2}\lim_{\delta\to 0}\delta^{-1}\left\langle E\left[\int_t^{t+\delta} I_\alpha(x,s) - \mu_\alpha(x) ds\right]\right\rangle \\ = & \sum_\beta \frac{j_{\alpha\beta}}{2}(w_{\alpha\beta} * \nu_\beta)(x). \end{aligned} \tag{15}$$

is the input variance, and $\xi(t)$ is zero-mean delta-correlated white noise. Here $w_{\alpha\beta}(x) \equiv q_\beta j_{\alpha\beta} k^{\Gamma}_{\alpha\beta}(x)$ is the distance (x)-dependent weighted connectivity, $\nu_\alpha(x) \equiv \langle E[s_{\alpha,k}]\rangle$ is the population- and position (x)-dependent mean firing rate, and $*$ indicates circular convolution, i.e. $(w_{\alpha\beta} * \nu_\beta)(x) \equiv \int_\Gamma w_{\alpha\beta}(x-x')v_\beta(x)dx'$.

Given input mean and variance, the firing rate of neurons of type α in position x is computed using a Fokker-Planck approach [36, 37]. For a given α and x, the variables $p_{s,\alpha}(x,V) = P_{s,\alpha}(x,V)/\nu_{s,\alpha}(x)$ and $j_{s,\alpha}(x,V) = J_{s,\alpha}(x,V)/\nu_{s,\alpha}(x)$, where $P_{s,\alpha}(x,V)$, $J_{s,\alpha}(x,V)$, and $\nu_{s,\alpha}(x)$ are the stationary probability distribution of the membrane potential, the current operator, and the firing rate, respectively, are described by

$$\begin{aligned} \frac{\partial p_{s,\alpha}}{\partial V}(x,V) &= \frac{1}{D_\alpha(x)}(M_{s,\alpha}(x,V)p_{s,\alpha}(x,V) - j_{s,\alpha}(x,V)), \\ \frac{\partial j_{s,\alpha}}{\partial V}(x,V) &= \delta(V - V_{\text{re}}). \end{aligned} \tag{16}$$

Here $M_{s,\alpha}(x,V) = \tau_\alpha^{-1}[g_{L,\alpha}(E_L - V) + \mu_\alpha(x)]$ is the drift coefficient. We integrate Eqs. 16 using a numerical integration scheme previously introduced [36], specifically using Simpson's rule [37]. The firing rate is then given by

$$\nu_{s,\alpha}(x) = \left[\int_{V_{\text{lb}}}^{V_{\text{th}}} p_{s,\alpha}(x,V)dV\right]^{-1}, \tag{17}$$

where the membrane potential lower bound V_{lb} is selected so that $P_{s,\alpha}(x, V_{\text{lb}})$ is negligible (here set to $V_{\text{lb}} = -1$).

This numerical integration scheme defines a mapping Φ from the input mean $\mu_\alpha(x)$ and variance $D_\alpha(x)$ to the position-dependent firing rate, defining a set of self-consistent equations $\nu_\alpha(x) = \Phi(\mu_\alpha(x), D_\alpha(x))$. Fixed

points are found using an iterative scheme as described in Ref. [37]. Starting from an initial guess $\nu_\alpha^{(0)}(x)$ for each α, $\mu_\alpha^{(0)}(x)$ and $D_\alpha^{(0)}(x)$ are computed using Eq. 2 and 15 and the next guess is computed iteratively,

$$\nu_\alpha^{(j)}(x) = \Phi(\mu_\alpha^{(j-1)}(x), D_\alpha^{(j-1)}(x)), \tag{18}$$

until the L2 deviation between $\nu_\alpha^{(j)}(x)$ and $\nu_\alpha^{(j-1)}(x)$ is less than a threshold, which we set to 10^{-7} Hz.

C. Balanced state in the thermodynamic limit

Theories of randomly connected neural networks sought to explain asynchronous spiking activity with models of a balanced state in which excitatory and inhibitory inputs dynamically achieve balance [35]. In this state, firing rates of neurons can be expressed in analytic form which becomes exact in the large-N limit. In Sec. II B we generalize the approach by Rosenbaum and Doiron [13] which implemented two populations—one excitatory and one inhibitory—for the four-population model where the inhibitory population is split into three subtypes. Here we provide details about derivation of Eq. 6 in Sec. II B.

Each component of $\tilde{W}$ in Eq. 5 can be written $\tilde{w}_{\alpha\beta} = q_\beta j_{\alpha\beta}\bar{k}_{\alpha\beta}\tilde{g}(n; 0, \sigma_{\beta f})$, where q_β, $j_{\alpha\beta}$, and $\bar{k}_{\alpha\beta}$ are constants independent of n and $\tilde{g}(n; 0, \sigma_{\beta f}) = e^{-2n^2\pi^2\sigma_{\beta f}^2}$ is the nth Fourier component of the wrapped Gaussian. We can thus write $\tilde{W} = \bar{J}S(n)$ where $S(n) = \mathrm{diag}[\tilde{g}(n; 0, \sigma_e), \tilde{g}(n; 0, \sigma_p), \tilde{g}(n; 0, \sigma_s), \tilde{g}(n; 0, \sigma_v)]$ and $\bar{J}_{\alpha\beta} = q_\beta j_{\alpha\beta}\bar{k}_{\alpha\beta}$, yielding $\det(\tilde{W}) = \det(\bar{J})\prod_{\beta'}\tilde{g}(n; 0, \sigma_{\beta'})$. The cofactors have a similar structure and can be written $\tilde{A}_{\alpha\beta} = \bar{B}_{\alpha\beta}\prod_{\beta''\neq\alpha}\tilde{g}(n; 0, \sigma_{\beta''})$, where $\bar{B}_{\alpha\beta}$ are cofactors of $\bar{J}$. Hence,

$$\begin{aligned}\tilde{\nu}_\alpha(n) &= \frac{\sum_\beta \bar{f}_\beta p_\alpha \tilde{g}(n; x_f, \sigma_{\beta f})\bar{B}_{\alpha\beta}\prod_{\beta''\neq\alpha}\tilde{g}(n; 0, \sigma_{\beta''})}{\det[\bar{J}]\prod_{\beta'}\tilde{g}(n; 0, \sigma_{\beta'})} \\ &= \sum_\beta \frac{\bar{f}_\beta p_\alpha \bar{B}_{\alpha\beta}}{\det[\bar{J}]}\cdot\frac{\tilde{g}(n; x_f, \sigma_{\beta f})}{\tilde{g}(n; 0, \sigma_\alpha)}.\end{aligned} \tag{19}$$

We note that because of the cancellation of factors $\tilde{g}(n; 0, \sigma_{\beta''})$ in Eq. 19, the spatial profile of population α will not depend on σ_β for $\beta \neq \alpha$, provided that the solution exists. In order to have $\lim_{n\to\infty}\tilde{\nu}_\alpha(n) = 0$, we must have $\sigma_{\beta f} > \sigma_\alpha$ for each α, β. If this is satisfied, the balanced solution can be written as

$$\nu_\alpha(x) = \bar{\nu}_\alpha^f + \sum_\beta \bar{\nu}_{\alpha\beta}^g g\left(x; 0, \sqrt{\sigma_{\beta f}^2 - \sigma_\alpha^2}\right) \tag{20}$$

where

$$\bar{\nu}_\alpha^f = \sum_\beta \frac{(1-p_\beta)\bar{f}_\beta\bar{B}_{\alpha\beta}}{\det[\bar{J}]}, \quad \bar{\nu}_{\alpha\beta}^g = \frac{p_\beta\bar{f}_\beta\bar{B}_{\alpha\beta}}{\det[\bar{J}]}. \tag{21}$$

For this to be a valid physical solution, the firing rates in Eq. 20 must be positive. This does not imply that each term in Eqs. 21 must be positive. The generalized solution admits solutions where some terms are negative, resulting in inverted (but positive) firing rate profiles.

Synaptic weights $j_{\alpha\beta}$ and external input intensities $\bar{f}_\alpha$ that achieve balance are generated numerically as follows. Synaptic weights are constrained to be in the range $[0.2, 2]$ and external inputs in the range $[10^{-5}, 10^{-1}]$. Initial values are generated randomly within the bounds and then the parameters are adjusted to minimize the mean square deviation between $\bar{\nu}_\alpha$ and target firing rates set at 50 Hz using the Sequential Least Squares Programming algorithm. If the resulting firing rates are all positive, the parameters are accepted. One such set of synaptic weights and external input parameters was used Figs. 1-4 and are listed in Table II. Parameters used in Fig. 5 are described in Sec. IV F.

D. Conductance-based model

When simulating conductance-based neurons, Eq. 10 becomes

$$I_{\alpha,k}(t) = \sum_{\beta\in\{e,p,s,v\}}\sum_{j=1}^{q_\beta N} J_{\alpha\beta}^{k,j}(E_\beta - V)s_{\beta,j}(t) + F_\alpha(x), \tag{22}$$

where E_β is the reversal potential, set to $E_e = 1.5$ for excitatory and $E_\beta = E_i = -0.5$ for inhibitory presynaptic neurons. For conductance-based equations, we replace E_L in Eq. 16 with the effective leak voltage $E'_{L,\alpha}$ which is dependent on cell type [36],

$$E'_{L,\alpha}(x) = \frac{E_L + \tau_\alpha\sum_\beta R_{\alpha\beta}(x)(b_{\alpha\beta} + b_{\alpha\beta}^2)E_\beta}{1 + \tau_\alpha\sum_\beta R_{\alpha\beta}(x)(b_{\alpha\beta} + b_{\alpha\beta}^2)} \tag{23}$$

and the membrane conductance $g_{L,\alpha}$ with

$$g'_{L,\alpha} = g_{L,\alpha}\left(1 + \tau_\alpha\sum_\beta R_{\alpha\beta}(x)(b_{\alpha\beta} + b_{\alpha\beta}^2)\right) \tag{24}$$

where $b_{\alpha\beta} = 1 - e^{-J_{\alpha\beta}}$ and $R_{\alpha\beta}$ is the input spike rate from population β, given by

$$R_{\alpha\beta}(x) = Nq_\beta(k_{\alpha\beta}^\Gamma * \nu_\beta)(x). \tag{25}$$

We use the same neuronal and synaptic parameters $g_{L,\alpha}$, τ_α, and $j_{\alpha\beta}$ as in the current-based case (Table II). We integrate Eqs. 16 as before, now with a voltage-dependent diffusion

$$D_\alpha(x, V) = \frac{1}{2}\left(\sum_\beta R_{\alpha\beta}(x)b_{\alpha\beta}^2(V - E_\beta)^2\right). \tag{26}$$

Due to inputs being voltage-dependent, the stability matrix $C(n) = \tilde{W} - \epsilon I$, where $\tilde{W}$ is the matrix with Fourier components $\tilde{w}_{\alpha\beta}(n)$, is also modified. We make the simplifying assumption that the mean membrane potential is independent of x, yielding

$$C(n) = \begin{pmatrix} -\epsilon + \tilde{w}_{ee}v_e^E & -\tilde{w}_{ep}v_e^I & -\tilde{w}_{es}v_e^I & -\tilde{w}_{ev}v_e^I \\ \tilde{w}_{pe}v_p^E & -\epsilon - \tilde{w}_{pp}v_p^I & -\tilde{w}_{ps}v_p^I & -\tilde{w}_{pv}v_p^I \\ \tilde{w}_{se}v_s^E & -\tilde{w}_{sp}v_s^I & \epsilon - \tilde{w}_{ss}v_s^I & -\tilde{w}_{sv}v_s^I \\ \tilde{w}_{ve}v_v^E & -\tilde{w}_{vp}v_v^I & -\tilde{w}_{vs}v_v^I & \epsilon - \tilde{w}_{vv}v_v^I \end{pmatrix} \tag{27}$$

where $v_\alpha^E = \bar{V}_\alpha - E_e$, $v_\alpha^I = \bar{V}_\alpha - E_i$, and $\bar{V}_\alpha = \int_\Gamma V_\alpha(x)dx$.

E. Spatiotemporal analysis

Temporal variance was computed to quantify the variability in population firing rates over time. For each simulation, spike times from individual populations were binned into 1 ms temporal windows over the analysis period (200 ms). Spike counts in each bin were converted to instantaneous firing rates (Hz) by dividing by the bin duration. The temporal variance was then calculated as the sample variance of this firing rate time series across all time bins within the analysis window. This procedure was repeated for 20 random seeds. For each σ_e value, the mean temporal variance was calculated by averaging across all seeds.

To estimate the peak spatial frequency of population activity, we first formed a spatial firing-rate profile by binning spikes across the position coordinate $x \in [0, 1]$ with bin width $\Delta x = 0.02$ and computing the firing rate within each bin. The mean was subtracted from the resulting spatial rate profile and its discrete spatial Fourier transform was computed via a Fast Fourier Transform (FFT). The one-sided spatial power spectrum was then formed by retaining only positive spatial frequencies (in cycles per unit distance). The peak spatial frequency was defined as the frequency with maximum power. This process was again repeated for the 20 random seeds.

F. Modulation of visual response

Modulations by specific inhibitory neuronal populations are measured by changes in the excitatory neurons' response to a visual stimulus. We first set $p_\alpha = 0$ in Eq. 13 to induce spatially uniform input $f_\alpha(x) = \bar{f}_\alpha$ and the network parameters $\bar{j}_{\beta\alpha}$ and $\bar{f}_\alpha$ are re-tuned to bring the network firing rate to below 10 Hz, which are the observed spontaneous firing rates in mouse V1 in the absence of visual stimuli [28]. The resulting parameters are listed in the Supplemental Material, Sec. 2. Visual stimuli and modulatory signals are given in addition to the baseline input.

The visual input is incorporated by an additional term $I_{v,\alpha}(x)$ to the total input given to the mean input in Eqs. 10 or 22. For the current-based model, this is given by

$$I_{v,\alpha}(x) = a_v \bar{v}_\alpha g(x; x_v, \sigma_v) \tag{28}$$

where a_v controls the overall strength of the visual input, $\bar{v}_\alpha$ is a population-dependent term controlling the relative strength of the visual input to population α, $x_v = 0.5$ is the center of the stimulus and $\sigma_v = 0.3$ is the spatial spread of the input. Feedforward visual inputs are known to be fed to E and PV neurons [26], so we set $\bar{v}_e = \bar{f}_e$, $\bar{v}_p = \bar{f}_p$, and $\bar{v}_s = \bar{v}_v = 0$.

For the conductance-based model, the visual stimuli are represented by conductance-based synaptic inputs. This results in an additional term in each of the summations over β in Eqs. 23, 24, 26 to include inputs from an external layer T where we set $R_{\alpha T}(x) = a_v r_\alpha g(x; x_v, \sigma_v)$ for $\alpha \in e, p$ and $R_{\alpha T} = 0$ otherwise. We set $r_e = 4 \times 10^{-4}$ and $r_p = 1 \times 10^{-4}$, values tuned to achieve realistic firing rate responses [28]. Synaptic weight parameters are set to $b_{eT} = 1 - e^{-0.2}$ and $b_{pT} = 1 - e^{-0.02}$.

To measure modulations, we first measure the excitatory response of the system to visual stimuli of varying intensity without additional activation of inhibitory neurons. This is done by computing the cell-type and position-dependent stationary firing rates $\nu_\alpha(x)$ for a_v varying from 0 to 12. Then the process is repeated with an additional current input given to a specific inhibitory cell type, similar to optogenetic stimulations in experimental studies [25, 28, 31]. The inhibition-activating stimulus is given by a Gaussian current input centered at x_C, which is set to $x_C = 0.5$ for proximal stimulations (Figs. 5b,d) and 0 for distal stimulations (Figs. 5c,e). The spatial spread of the inhibition-activating input is given by the standard deviation $\sigma_C = 0.2$ and the magnitude is set equal to $\bar{f}_{\alpha C}$, i.e., $f_C(x) = \bar{f}_\alpha g(x; x_C, \sigma_C)$. In the current-based model, $\bar{f}_{\alpha C}$ was first set to $\bar{f}_\alpha$ and then increased until the modulation partially silenced at least one population in order to induce nonlinear effects–otherwise, no gain modulations were observed. In the conductance-based model, the effects of modulation were stronger and the modulation was decreased if complete suppression of responses occurred. Parameters are listed in the Supplemental Materials, Sec. 2. The mean visual response (dots in Figs. 5d-e) is defined as the mean excitatory firing rate in the range $[x_f - \sigma_v, x_f + \sigma_v]$, i.e.,

$$\int^{\text{vis}} \nu_e(x)dx \equiv \int_{x_v - \sigma_v}^{x_f + \sigma_v} \nu_e(x)dx. \tag{29}$$

G. Linear response theory

Linear responses to input perturbations are computed with the methods developed in Refs. [36, 37] and briefly outlined here. Linear responses are measured for excitatory neurons at position $x = 0.5$; cell type indices and positions are suppressed in the following equations. If a weak noise term $\sqrt{2D}\xi(t)$ is added to the visual input

$I_v(t)$ (we set $D = 0.1$), the cross-spectral density is given by

$$\tilde{C}(f) = 2DS_\nu(f) \tag{30}$$

where $S_\nu(f)$ is the susceptibility function of the firing rate. We consider a perturbation to the visual input

$$I_v(t) = I_{v,s}(t) + \varepsilon e^{2\pi i f t} \tag{31}$$

where $I_{v,s}(t)$ is the unperturbed input to the neuron, f is the frequency of the modulation and ε is a small parameter controlling the amplitude of the modulation. Setting $\varepsilon = 0$ recovers the fixed-point solution. To first order in ε, the response of the neuron is periodic with frequency f,

$$\begin{aligned} P(V,t) &= P_s(V) + \varepsilon P_t(V) e^{2\pi i f t} \\ \nu(t) &= \nu_s + \varepsilon S_\nu(f) e^{2\pi i f t} \end{aligned}$$

where $P_s(V)$ and ν_s are the steady-state probability density function and the firing rate, respectively, and $P_t(V)$ and $S_\nu(f)$ are the susceptibility functions. From here a time-dependent Fokker-Plank equation for the probability density $P(V,t)$ can be derived with a drift coefficient

$$M(V,t) = M_s(V) + \varepsilon M_t e^{2\pi i f t} \tag{32}$$

where $M_s(V)$ is the stationary drift coefficient in Eq. 16 and M_t is the coefficient of the time-dependent drift, given by $M_t = g_{L,\alpha}\tau_\alpha$. We can decompose the probability density and flux functions as $P_t(V) = S_\nu p_\nu(V) + p_t(V)$ and $J_t(V) = S_\nu j_\nu(V) + j_t(V)$ which satisfy the equations

$$\begin{aligned} -\frac{\partial p_t}{\partial V} &= -\frac{1}{D} M_s p_t + \frac{1}{D}[j_t - M_t p_s] \\ -\frac{\partial j_t}{\partial V} &= 2\pi i f p_t \\ -\frac{\partial p_\nu}{\partial V} &= -\frac{1}{D} M_s p_\nu + \frac{1}{D} j_\nu \\ -\frac{\partial j_\nu}{\partial V} &= 2\pi i f p_\nu - \delta(V - V_{\mathrm{re}}) \end{aligned} \tag{33}$$

with boundary conditions $p_\nu(V_{\mathrm{th}}) = p_t(V_{\mathrm{th}}) = j_t(V_{\mathrm{th}}) = 0$ and $j_\nu(V_{\mathrm{th}}) = 1$. We integrate these equations with Simpson's rule to obtain the susceptibility,

$$S_\nu = -\frac{j_t(V_{\mathrm{lb}})}{j_\nu(V_{\mathrm{lb}})} \tag{34}$$

where V_{lb} is the lower bound of the membrane potential, set to -1. The cross-spectral density is then computed using Eq. 30.

Data, Materials, and Software Availability

All code used in this study is available on GitHub at https://github.com/HChoiLab/CellTypeMeanField.

ACKNOWLEDGMENTS

This work was supported by the National Eye Institute of the National Institutes of Health under Award Number R00 EY030840. The content is solely the responsibility of the authors and does not necessarily represent the official views of the National Institutes of Health.

[1] B. Haider, A. Duque, A. R. Hasenstaub, and D. A. McCormick, Neocortical network activity in vivo is generated through a dynamic balance of excitation and inhibition, Journal of Neuroscience **26**, 4535 (2006).
[2] M. Okun and I. Lampl, Instantaneous correlation of excitation and inhibition during ongoing and sensory-evoked activities, Nature Neuroscience **11**, 535 (2008).
[3] B. V. Atallah and M. Scanziani, Instantaneous modulation of gamma oscillation frequency by balancing excitation with inhibition, Neuron **62**, 566 (2009).
[4] T. P. Carvalho and D. V. Buonomano, Differential effects of excitatory and inhibitory plasticity on synaptically driven neuronal input-output functions, Neuron **61**, 774 (2009).
[5] J. A. Cardin, Inhibitory interneurons regulate temporal precision and correlations in cortical circuits, Trends in Neurosciences **41**, 689 (2018).
[6] J. S. Isaacson and M. Scanziani, How inhibition shapes cortical activity, Neuron **72**, 231 (2011).
[7] K. A. Ferguson and J. A. Cardin, Mechanisms underlying gain modulation in the cortex, Nature Reviews Neuroscience **21**, 80 (2020).
[8] C. Van Vreeswijk and H. Sompolinsky, Chaos in neuronal networks with balanced excitatory and inhibitory activity, Science **274**, 1724 (1996).
[9] M. Ercsey-Ravasz, N. T. Markov, C. Lamy, D. C. Van Essen, K. Knoblauch, Z. Toroczkai, and H. Kennedy, A predictive network model of cerebral cortical connectivity based on a distance rule, Neuron **80**, 184 (2013).
[10] Petilla terminology: nomenclature of features of gabaergic interneurons of the cerebral cortex, Nature Reviews Neuroscience **9**, 557 (2008).
[11] R. Tremblay, S. Lee, and B. Rudy, Gabaergic interneurons in the neocortex: from cellular properties to circuits, Neuron **91**, 260 (2016).

[12] N. T. Markov, M. Ercsey-Ravasz, C. Lamy, A. R. Ribeiro Gomes, L. Magrou, P. Misery, P. Giroud, P. Barone, C. Dehay, Z. Toroczkai, *et al.*, The role of long-range connections on the specificity of the macaque interareal cortical network, Proceedings of the National Academy of Sciences **110**, 5187 (2013).

[13] R. Rosenbaum and B. Doiron, Balanced networks of spiking neurons with spatially dependent recurrent connections, Physical Review X **4**, 021039 (2014).

[14] R. Pyle and R. Rosenbaum, Spatiotemporal dynamics and reliable computations in recurrent spiking neural networks, Physical Review Letters **118**, 018103 (2017).

[15] R. Rosenbaum, M. A. Smith, A. Kohn, J. E. Rubin, and B. Doiron, The spatial structure of correlated neuronal variability, Nature Neuroscience **20**, 107 (2017).

[16] C. K. Pfeffer, M. Xue, M. He, Z. J. Huang, and M. Scanziani, Inhibition of inhibition in visual cortex: the logic of connections between molecularly distinct interneurons, Nature Neuroscience **16**, 1068 (2013).

[17] L. Campagnola, S. C. Seeman, T. Chartrand, L. Kim, A. Hoggarth, C. Gamlin, S. Ito, J. Trinh, P. Davoudian, C. Radaelli, *et al.*, Local connectivity and synaptic dynamics in mouse and human neocortex, Science **375**, eabj5861 (2022).

[18] A. Litwin-Kumar, R. Rosenbaum, and B. Doiron, Inhibitory stabilization and visual coding in cortical circuits with multiple interneuron subtypes, Journal of neurophysiology **115**, 1399 (2016).

[19] J. H. Lee, C. Koch, and S. Mihalas, A computational analysis of the function of three inhibitory cell types in contextual visual processing, Frontiers in Computational Neuroscience **11**, 28 (2017).

[20] K. A. Wilmes, M. A. Petrovici, S. Sachidhanandam, and W. Senn, Uncertainty-modulated prediction errors in cortical microcircuits, bioRxiv , 2023 (2023).

[21] H. Bos, C. Miehl, A.-M. M. Oswald, and B. Doiron, Untangling stability and gain modulation in cortical circuits with multiple interneuron classes, eLife **13**, RP99808 (2025).

[22] R. A. Silver, Neuronal arithmetic, Nature Reviews Neuroscience **11**, 474 (2010).

[23] H. Adesnik, W. Bruns, H. Taniguchi, Z. J. Huang, and M. Scanziani, A neural circuit for spatial summation in visual cortex, Nature **490**, 226 (2012).

[24] N. R. Wilson, C. A. Runyan, F. L. Wang, and M. Sur, Division and subtraction by distinct cortical inhibitory networks in vivo, Nature **488**, 343 (2012).

[25] B. V. Atallah, W. Bruns, M. Carandini, and M. Scanziani, Parvalbumin-expressing interneurons linearly transform cortical responses to visual stimuli, Neuron **73**, 159 (2012).

[26] S. El-Boustani, N. R. Wilson, C. A. Runyan, and M. Sur, El-boustani et al. reply, Nature **508**, E3 (2014).

[27] S.-H. Lee, A. C. Kwan, and Y. Dan, Interneuron subtypes and orientation tuning, Nature **508**, E1 (2014).

[28] J. Del Rosario, S. Coletta, S. H. Kim, Z. Mobille, K. Peelman, B. Williams, A. J. Otsuki, A. D. C. Valerio, K. Worden, L. T. Blanpain, *et al.*, Lateral inhibition in v1 controls neural & perceptual contrast sensitivity, Nature Neuroscience (2025).

[29] F. Scala, D. Kobak, S. Shan, Y. Bernaerts, S. Laturnus, C. R. Cadwell, L. Hartmanis, E. Froudarakis, J. R. Castro, Z. H. Tan, *et al.*, Layer 4 of mouse neocortex differs in cell types and circuit organization between sensory areas, Nature Communications **10**, 4174 (2019).

[30] N. W. Gouwens, S. A. Sorensen, F. Baftizadeh, A. Budzillo, B. R. Lee, T. Jarsky, L. Alfiler, K. Baker, E. Barkan, K. Berry, *et al.*, Integrated morphoelectric and transcriptomic classification of cortical gabaergic cells, Cell **183**, 935 (2020).

[31] J. Veit, G. Handy, D. P. Mossing, B. Doiron, and H. Adesnik, Cortical vip neurons locally control the gain but globally control the coherence of gamma band rhythms, Neuron **111**, 405 (2023).

[32] M. M. Parker, J. E. Rubin, and C. Huang, State modulation in spatial networks with three interneuron subtypes, Science Advances **11**, eads9134 (2025).

[33] H. K. Kato, S. K. Asinof, and J. S. Isaacson, Network-level control of frequency tuning in auditory cortex, Neuron **95**, 412 (2017).

[34] R. Khajeh, F. Fumarola, and L. Abbott, Sparse balance: Excitatory-inhibitory networks with small bias currents and broadly distributed synaptic weights, PLOS Computational Biology **18**, e1008836 (2022).

[35] C. van Vreeswijk and H. Sompolinsky, Chaotic balanced state in a model of cortical circuits, Neural Computation **10**, 1321 (1998).

[36] M. J. Richardson, Firing-rate response of linear and nonlinear integrate-and-fire neurons to modulated current-based and conductance-based synaptic drive, Physical Review E **76**, 021919 (2007).

[37] R. Rosenbaum, A diffusion approximation and numerical methods for adaptive neuron models with stochastic inputs, Frontiers in Computational Neuroscience **10**, 39 (2016).

[38] N. Brunel, Dynamics of sparsely connected networks of excitatory and inhibitory spiking neurons, Journal of Computational Neuroscience **8**, 183 (2000).

[39] O. Harish and D. Hansel, Asynchronous rate chaos in spiking neuronal circuits, PLoS computational biology **11**, e1004266 (2015).

[40] F. S. Chance, L. F. Abbott, and A. D. Reyes, Gain modulation from background synaptic input, Neuron **35**, 773 (2002).

[41] C. Kehrer, N. Maziashvili, T. Dugladze, and T. Gloveli, Altered excitatory-inhibitory balance in the nmda-hypofunction model of schizophrenia, Frontiers in Molecular Neuroscience **1**, 226 (2008).

[42] J.-M. Fritschy, Epilepsy, e/i balance and gabaa receptor plasticity, Frontiers in Molecular Neuroscience **1**, 201 (2008).

[43] S. B. Nelson and V. Valakh, Excitatory/inhibitory balance and circuit homeostasis in autism spectrum disorders, Neuron **87**, 684 (2015).

[44] H. S. Seung and U. Sümbül, Neuronal cell types and connectivity: lessons from the retina, Neuron **83**, 1262 (2014).

[45] C. Teeter, R. Iyer, V. Menon, N. Gouwens, D. Feng, J. Berg, A. Szafer, N. Cain, H. Zeng, M. Hawrylycz, *et al.*, Generalized leaky integrate-and-fire models classify multiple neuron types, Nature Communications **9**, 709 (2018).

[46] C. N. Winston, D. Mastrovito, E. Shea-Brown, and S. Mihalas, Heterogeneity in neuronal dynamics is learned by gradient descent for temporal processing tasks, Neural Computation **35**, 555 (2023).

[47] R. Gast, S. A. Solla, and A. Kennedy, Macroscopic dynamics of neural networks with heterogeneous spiking

thresholds, Physical Review E **107**, 024306 (2023).

[48] R. Gast, S. A. Solla, and A. Kennedy, Neural heterogeneity controls computations in spiking neural networks, Proceedings of the National Academy of Sciences **121**, e2311885121 (2024).

[49] B. Hellwig, A quantitative analysis of the local connectivity between pyramidal neurons in layers 2/3 of the rat visual cortex, Biological cybernetics **82**, 111 (2000).

[50] P. Buzás, K. Kovács, A. S. Ferecskó, J. M. Budd, U. T. Eysel, and Z. F. Kisvárday, Model-based analysis of excitatory lateral connections in the visual cortex, Journal of Comparative Neurology **499**, 861 (2006).

[51] N. Voges and L. Perrinet, Complex dynamics in recurrent cortical networks based on spatially realistic connectivities, Frontiers in computational neuroscience **6**, 41 (2012).

[52] R. B. Levy and A. D. Reyes, Spatial profile of excitatory and inhibitory synaptic connectivity in mouse primary auditory cortex, Journal of Neuroscience **32**, 5609 (2012).

[53] M. W. Reimann, A.-L. Horlemann, S. Ramaswamy, E. B. Muller, and H. Markram, Morphological diversity strongly constrains synaptic connectivity and plasticity, Cerebral Cortex **27**, 4570 (2017).

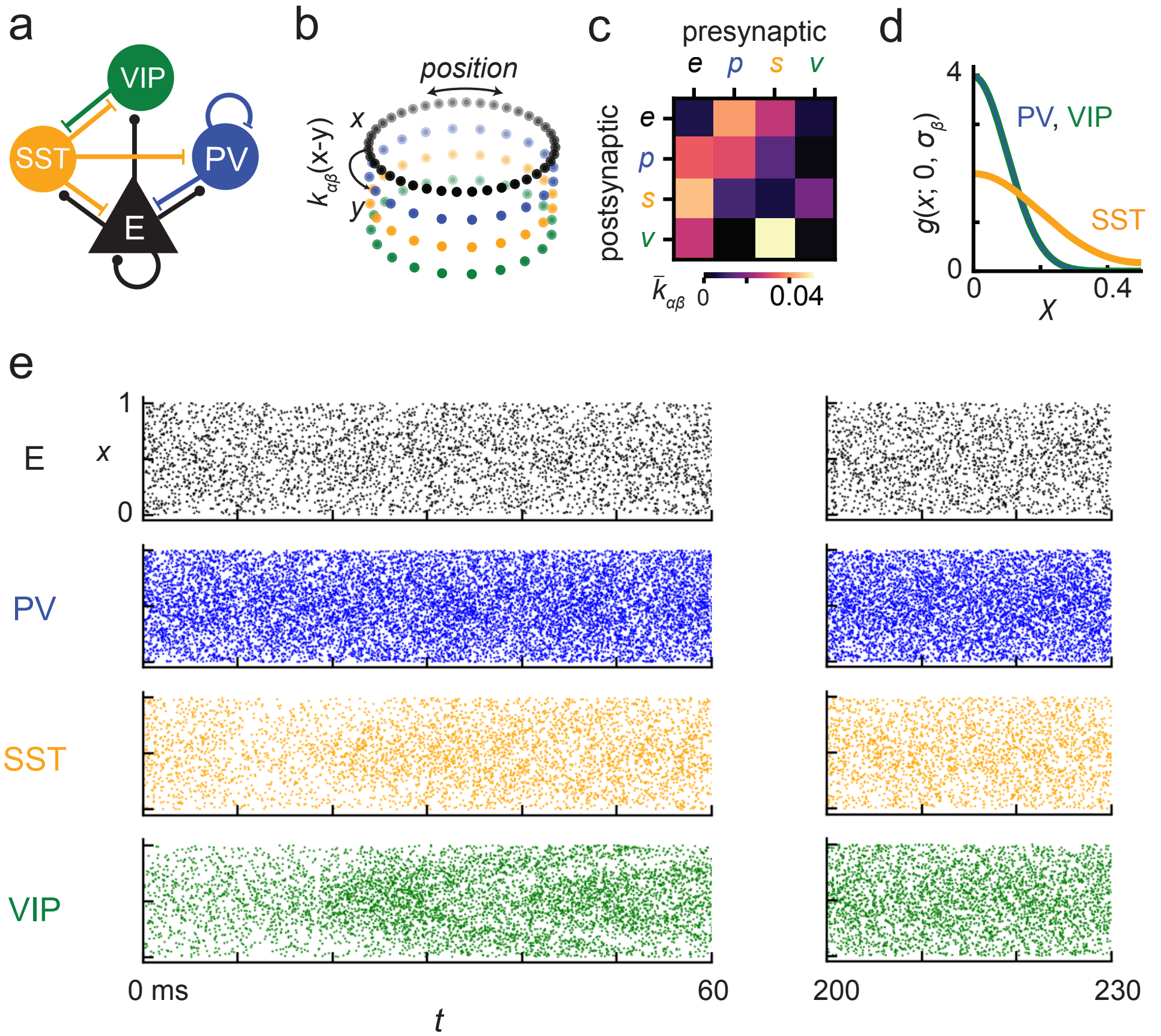
a
VIP
SST
PV
E
b
position
x
y
$k_{\alpha\beta}(x-y)$
c
presynaptic
e p s v
postsynaptic
e
p
s
v
$\bar{k}_{\alpha\beta}$ 0
0.04
d
4
0
PV, VIP
SST
$g(x; 0, \sigma_\beta)$
0
0.4
x
e
E
x
1
0
PV
SST
VIP
0 ms
60
200
230
t

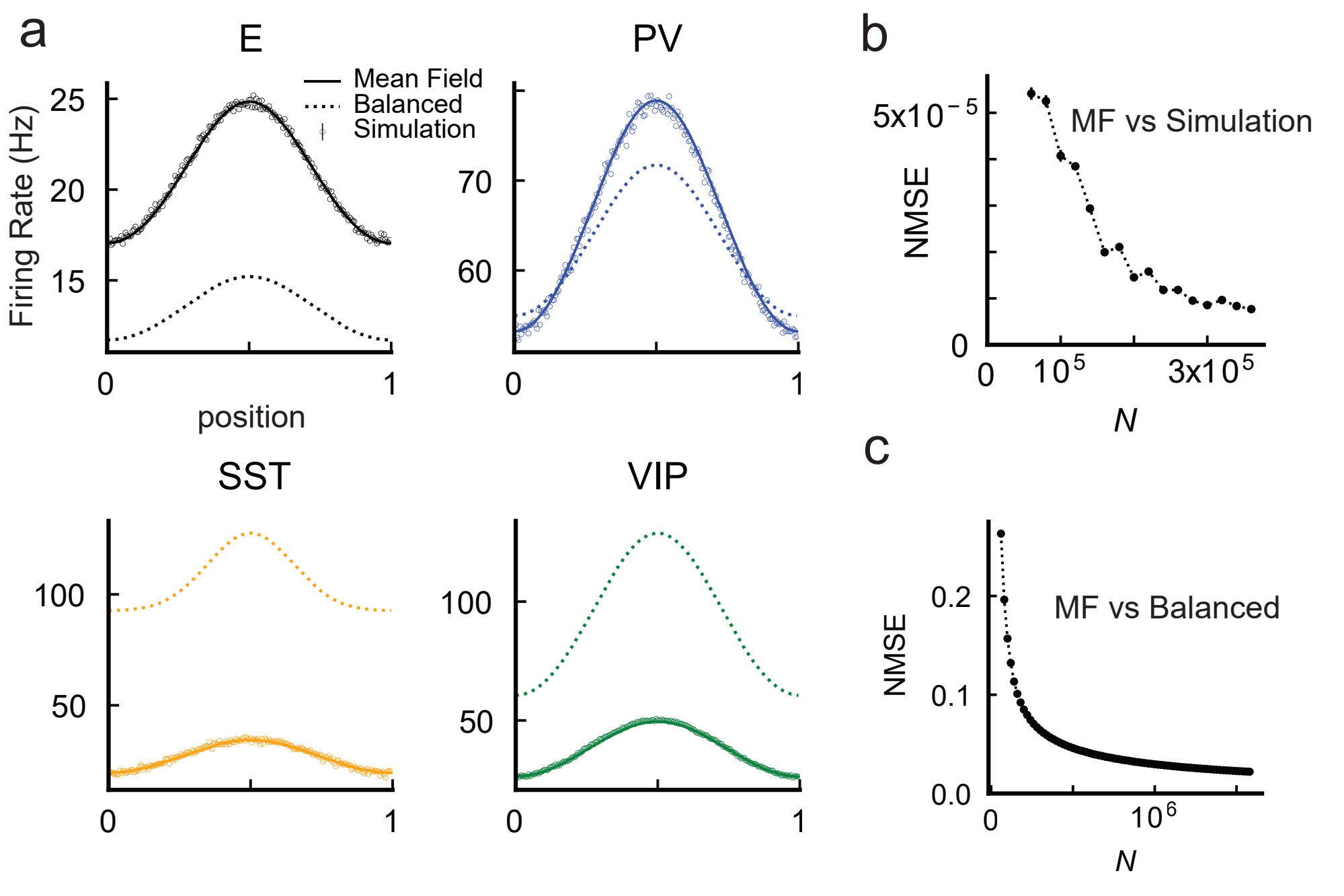
a
E
PV
SST
VIP
Mean Field
Balanced
Simulation
Firing Rate (Hz)
25
20
15
70
60
100
50
0
1
position
b
MF vs Simulation
NMSE
5x10^{-5}
0
10^5
3x10^5
N
c
MF vs Balanced
NMSE
0.2
0.1
0.0
10^6
N

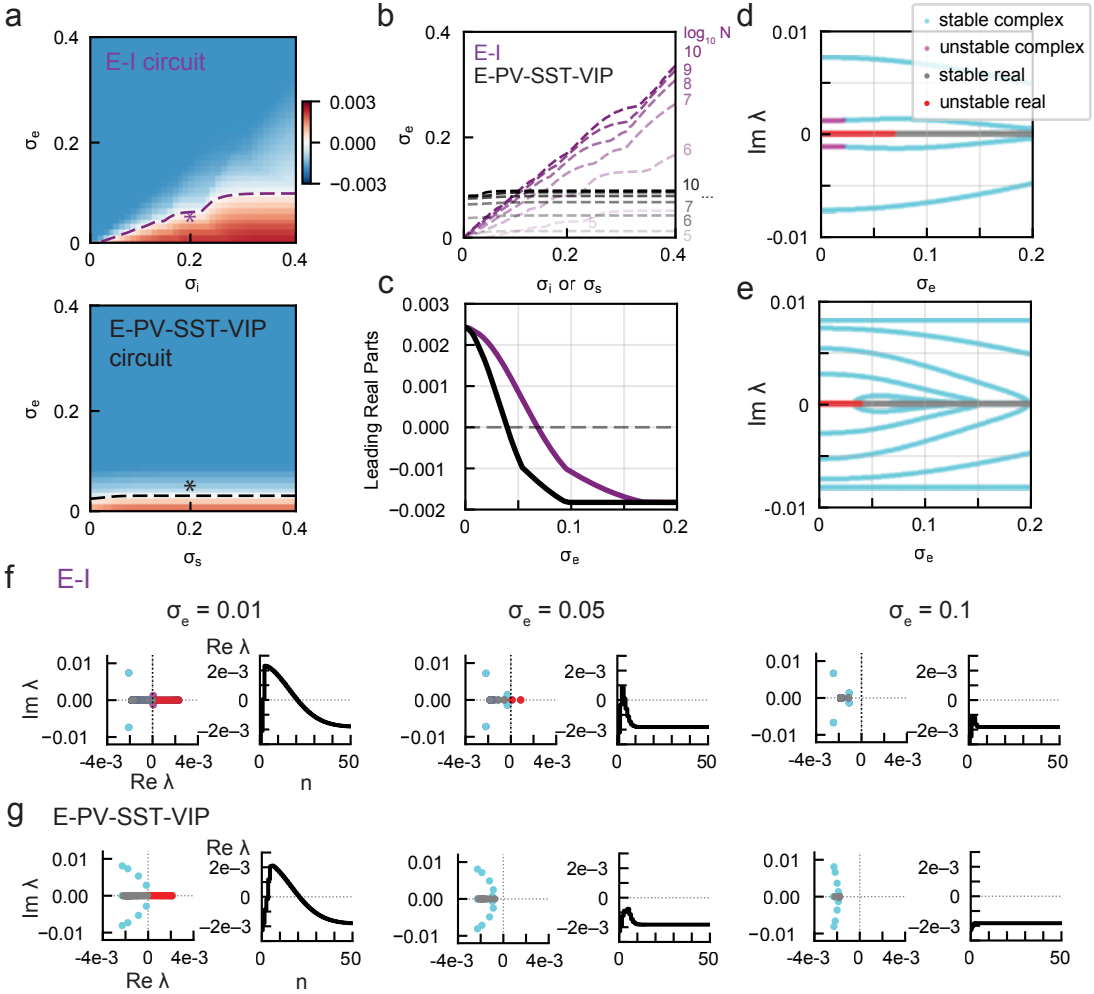
a
E-I circuit
σe
σi
0.003
0.000
−0.003
E-PV-SST-VIP circuit
σs
b
E-I
E-PV-SST-VIP
log10 N
σi or σs
c
Leading Real Parts
σe
d
stable complex
unstable complex
stable real
unstable real
Im λ
e
f
E-I
σe = 0.01
σe = 0.05
σe = 0.1
Re λ
n
g
E-PV-SST-VIP

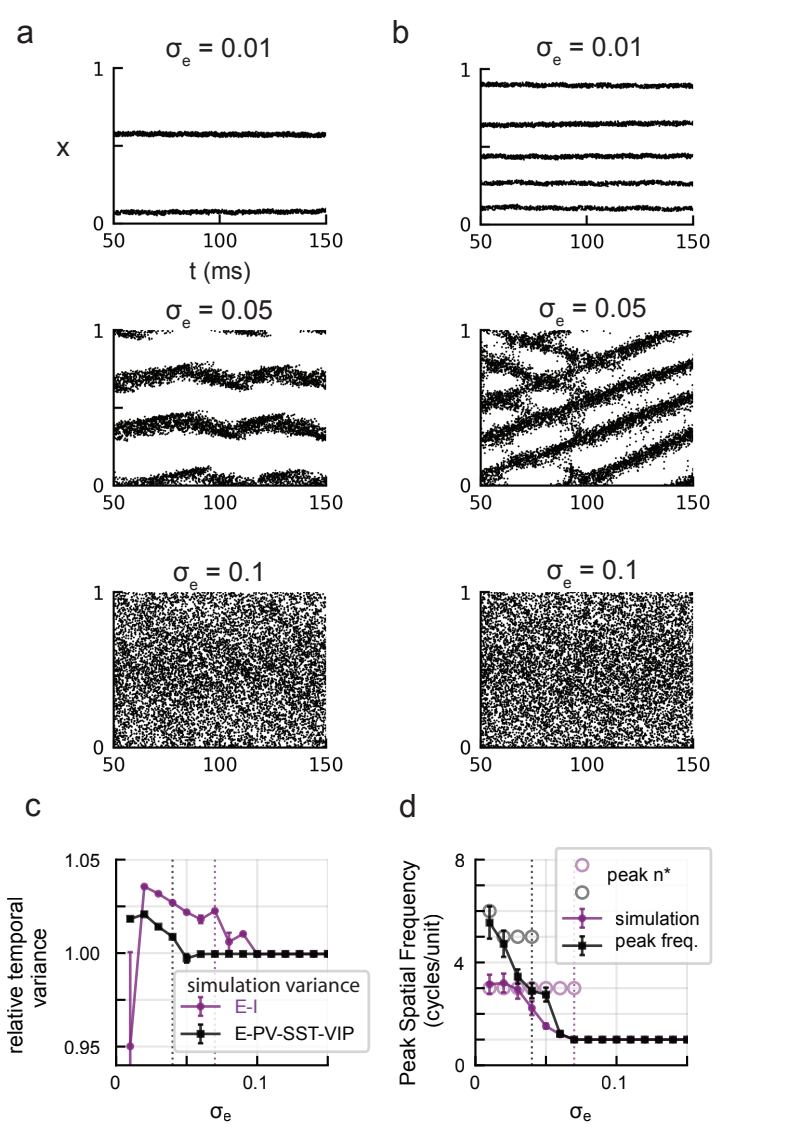
a
b
σe = 0.01
σe = 0.05
σe = 0.1
x
t (ms)
c
d
relative temporal variance
simulation variance
E-I
E-PV-SST-VIP
Peak Spatial Frequency (cycles/unit)
peak n*
simulation peak freq.
σe

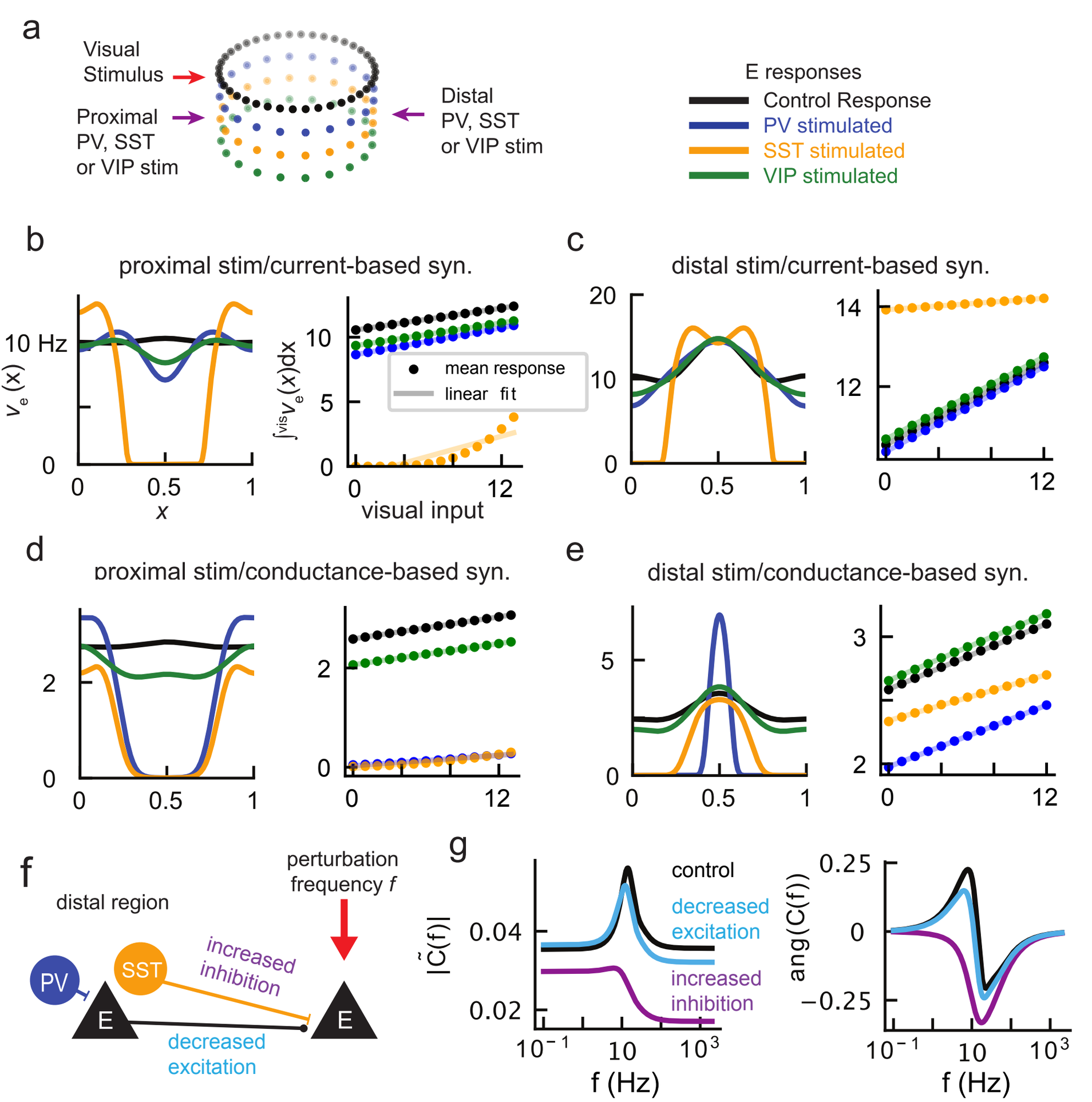
a
Visual Stimulus
Proximal PV, SST or VIP stim
Distal PV, SST or VIP stim
E responses
Control Response
PV stimulated
SST stimulated
VIP stimulated
b
proximal stim/current-based syn.
10 Hz
$\nu_e(x)$
x
$\int^{vis} \nu_e(x)dx$
mean response
linear fit
visual input
c
distal stim/current-based syn.
d
proximal stim/conductance-based syn.
e
distal stim/conductance-based syn.
f
distal region
perturbation frequency f
PV
SST
E
E
increased inhibition
decreased excitation
g
control
decreased excitation
increased inhibition
$|\tilde{C}(f)|$
ang(C(f))
f (Hz)
f (Hz)